Chapter 4
The Embedded-Atom Method

Arthur F. Voter
Theoretical Division, Los Alamos National Laboratory, Los Alamos, NM 87545, USA

1. Introduction

The use of atomistic simulation methods is becoming increasingly common in materials science. Because computer speeds continue to increase, simulations are being designed that more and more closely approximate real materials systems and processes. Using molecular dynamics (MD), in which a classical trajectory is integrated for a period of time, the fastest computers available today allow one to evolve a system of 10^6 atoms for a fraction of a nanosecond. This system size and duration is more than sufficient for modeling many material properties, especially equilibrium properties. In about 10 more years, direct simulation of fracture in three dimensions should be feasible for a system of 10^9–10^{10} atoms.

Besides system size and run duration, a key factor in making a connection to reality is the accuracy of the model for the interatomic forces. The properties predicted by an atomistic simulation are only as good as the quality of the underlying interatomic potential. The focus of this chapter is the embedded-atom method (EAM), a recently developed form of interatomic potential that has led to considerable improvement in the quality of predictions for metals and intermetallics.

It is important to state at the outset that EAM is a semiempirical approach. If highly accurate, first-principles results are desired, one can employ a quantum-chemical or density-functional method. However, these approaches are much more expensive, with computational work scaling as the number of atoms (n) to the third power or worse. Currently, simulations with these approaches are restricted to less than 100 atoms. The virtue of the EAM is that it scales as n, requiring only 2–5 times the work of a pair-potential model, yet includes some many-body effects that are important for the description of metallic systems. Although the development of more complex, more accurate potentials is an active area of research, there will always be a need for fast, n-scaling potentials such as the EAM form because some simulation studies benefit from using the largest possible system.

The goal of this chapter is to offer an introduction to the embedded atom method and its use in atomistic simulations. No attempt is made to give a comprehensive survey of EAM results for intermetallic compounds. Rather, it is intended to be a sort of 'users' guide' to EAM, and to provide some historical and physical perspective. Loosely, the flow is as follows: (a) present the mathematical form of EAM and discuss its merits for computational simulations; (b) discuss the origins of EAM, and its physical interpretation; (c) discuss the equivalent methods that go by different names; (d) give a detailed description of how one goes about fitting an EAM potential for both pure elements and intermetallic alloys; (e) give examples of properties that can be calculated with EAM; and (f) discuss the limitations of EAM for modeling intermetallic compounds.

2. The Embedded-Atom Method

2.1 Energy Expression for Pure Elements

In any n-scaling energy expression, the total energy (E_{tot}) of a system of n atoms can be written as a sum over atom energies:

Intermetallic Compounds: Vol. 1, *Principles*. Edited by J. H. Westbrook and R. L. Fleischer

$$E_{\text{tot}} = \sum_{i}^{n} E_i \tag{1}$$

In the embedded-atom method (EAM), proposed by Daw and Baskes (1983, 1984), E_i is given by

$$E_i = \tfrac{1}{2}\sum_j \phi(r_{ij}) + F(\bar{\rho}_i) \tag{2}$$

with

$$\bar{\rho}_i = \sum_j \rho(r_{ij}) \tag{3}$$

Here r_{ij} is the scalar distance between atom i and atom j, ϕ is the pairwise interaction between atoms, ρ is another pairwise interaction leading to the 'density' term $\bar{\rho}_i$, and $F(\bar{\rho})$ is the 'embedding function.' The sums over neighboring atoms (j) are limited by the range of the cutoff for ϕ and ρ, which is generally one to four neighbor shells in the perfect crystal.

The computational procedure for evaluating the EAM energy is similar to that for a pair potential. For atom i, both $\phi(r_{ij})$ and $\rho(r_{ij})$ are summed over neighbors j, and then a single evaluation of $F(\bar{\rho}_i)$ is performed. Evaluation of the energy derivatives necessary for MD is only slightly more complicated. As with a pair potential, it is the radial cutoff of $\phi(r)$ and $\rho(r)$ that causes the total computational work to scale as n.

The physical interpretation of EAM is discussed in the next section, but some observations are made here about the general form. It is reasonable to think of $\bar{\rho}_i$ as a measure of the atomic density in the neighborhood of atom i, which, in turn, requires that $\rho(r_{ij})$ be a monotonically decreasing function of r_{ij}. In this sense, EAM can be thought of as a generalization of the fixed-volume pair potentials (Harrison, 1966), in which the 'volume' is now defined for each atom rather than the whole system. This allows treatment of defects for which the volume is ill-defined, such as free surfaces.

The key to EAM is the nonlinearity of the function $F(\bar{\rho})$. If F were purely linear, the two terms in equation (2) could be collapsed to give a simple pair potential. A nonlinear $F(\bar{\rho})$ thus provides a many-body contribution to the energy. Because $\bar{\rho}_i$ depends only on scalar distances to neighboring atoms, the many-body term has no angular dependence. Nonetheless, this spherically symmetric, many-body interaction is quite important. For example, with a simple pair potential, the vacancy formation energy is formally equivalent to the atomic cohesive energy, and the Cauchy pressure ($C_{12}-C_{44}$) is zero. Both of these conditions are non-physical for transition metals, and are remedied in the EAM expression.

2.2 Physical Interpretation of EAM

The embedded atom method has its roots in density-functional theory (DFT). The basis of DFT is that one can prove that the energy of a system of atoms is given exactly by a functional of its electronic density (Hohenberg and Kohn, 1964). Although the exact form of this functional may never be known, approximations to it can be derived, and have been employed with considerable success in studying the electronic structure of molecules and crystals. In a similar fashion, one can prove that the energy change associated with placing (embedding) an atom into a host system of atoms is a functional of the electronic density of the host system before the new atom is embedded (Stott and Zaremba, 1980; Norskov and Lang, 1980). If a good approximation to this embedding functional exists, one can envision constructing an approximate energy expression by viewing an atom in a solid as being embedded in the host density due to all the other atoms. The host density can be approximated by the superposition of atomic-charge distributions for each host atom. To zeroth order, the embedding energy can be equated to the energy of embedding an atom in a homogeneous electron gas, whose density ($\bar{\rho}$) matches the host density at the position of the embedded atom, augmented by the classical electrostatic interaction with the atoms in the host system. The embedding energy for the homogeneous electron gas can be calculated from first principles (Puska *et al.*, 1981). Computing $\bar{\rho}$ from a weighted average of the host density over the spatial extent of the embedded atom improves the description by accounting for the local inhomogeneity of the host density. The classical electrostatic interaction reduces to a pairwise sum if a frozen atomic charge density is assumed for each host atom. This approach, termed the quasiatom method (Stott and Zaremba, 1980) or effective-medium theory (Norskov and Lang, 1980), provided the conceptual platform for the development of EAM and EAM-like methods. Norskov (1982) used this approach to calculate the energy of hydrogen and helium impurities in various metals, obtaining good agreement with experimental trends.

Building on this, Daw and Baskes (1983) proposed two modifications: (1) replace the first-principles estimates of the terms in the energy expression with easily parameterizable forms for the electrostatic interaction ($\phi(r)$) and the embedding energy ($F(\bar{\rho})$); and (2) compute the embedding and electrostatic energy for each atom in the solid, summing them to obtain the total energy. Implicit in this treatment is a double

counting, owing to the fact that each atom acts as a host for, and is also hosted by, each other atom. (Manninen (1986) has since shown that this double counting error drops out if $\rho(r)$ is taken to be a transform of the actual density function.) Using the electron density from an atomic Hartree-Fock calculation (Clementi and Roetti, 1974) to define $\rho(r)$, the shapes for $\phi(r)$ and $F(\bar{\rho})$ were then optimized by fitting to experimental properties, resulting in a powerful semi-empirical approach.

More recently, the connection between EAM and local-density theory has been explored further, putting EAM on firmer theoretical footing, and spawning related, advanced potential forms; see, for example, Manninen (1986), Jacobsen *et al.* (1987), Kress and DePristo (1987, 1988), and Daw (1989).

To summarize, the physical interpretation of EAM from the viewpoint of effective-medium theory is as follows: $\rho(r)$ is essentially the electronic density as a function of distance from the nucleus of the atom; $\bar{\rho}_i$, which has been summed over neighbors of atom i, corresponds to the density of the host system with atom i removed; $F(\bar{\rho}_i)$ is the quantum-mechanical energy of embedding atom i into a homogeneous electron gas of density $\bar{\rho}_i$; and $\phi(r_{ij})$ is the classical electrostatic interaction between atoms i and j (and other correction terms).

There is also a simpler way to view the EAM form that is often useful. The many-body effect of $F(\bar{\rho})$ is that, as an atom makes more bonds, each new bond is weaker than the previous one; making a new bond increases the total bonding energy, but decreases the average energy per bond. This is consistent with traditional chemical bonding concepts. In this view, $\rho(r)$ plays the role of a bond sensor, which should decrease monotonically with r, and $\bar{\rho}_i$ offers a measure of the total bond order. The desired inverse correlation between bond order and bond length arises naturally because the bond order of an atom can increase by making either more bonds or shorter bonds. The weakening of successive bonds will occur if $F(\bar{\rho})$ has a positive curvature ($d^2F/d\bar{\rho}^2 > 0$). The first-principles determination of the energy for embedding an atom in a homogeneous electron gas (Puska *et al.*, 1981) indeed shows a positive curvature for all atoms that can make chemical bonds (i.e. all but the noble gas atoms, which show no curvature). Semiempirically fitted EAM potentials also show positive curvature in $F(\bar{\rho})$, as can be seen in Figure 1.

For a solid at equilibrium, the force to expand (or contract) due to the embedding function is exactly balanced by the force to contract (or expand) due to the pairwise interactions. At a defect, this balance is disrupted, leading to displacements as the atoms move to seek a new balance. The positive curvature of F plays a key role in this process, by defining the optimum tradeoff between the number of bonds and the lengths of those bonds. This leads to physically reasonable relaxations, as discussed for free surfaces in Section 5.1. While the curvature of F has physical significance in the many-body nature of the EAM potential, the *slope* of F does not. This is because changing the slope of F is equivalent to changing the pair potential, as will be shown in the next section (see equation (8)).

It is interesting to note that if one derives the elastic constants for the EAM energy expression (Daw and Baskes, 1984), the Cauchy pressure for a cubic crystal is found to depend directly on the curvature of F:

$$C_{12} - C_{44} = \frac{1}{\Omega} \frac{d^2F}{d\bar{\rho}_i^2} \left(\sum_j \frac{d\rho}{dr_{ij}} \frac{x_{ij}^2}{r_{ij}} \right)^2 \tag{4}$$

Here Ω is the atomic volume, x_{ij} is the Cartesian projection of r_{ij}, and one unique atom has been assumed for simplicity. Thus, for EAM potentials that maintain the chemically meaningful property that successive bonds are weaker, the Cauchy pressure cannot be negative. This implies that the negative Cauchy pressure exhibited by some transition metals (Ir, Rh) arises from directional bonding effects not included in EAM. A good description of these systems would require a potential with angular interactions.

2.3 EAM Energy Expression for Alloys

For an ordered alloy, or any system with more than one type of atom, the EAM energy expression in equation (2) is rewritten as

$$E_i = \tfrac{1}{2} \sum_j \phi_{t_i t_j}(r_{ij}) + F_{t_i}(\bar{\rho}_i) \tag{5}$$

with

$$\bar{\rho}_i = \sum_j \rho_{t_j}(r_{ij}) \tag{6}$$

Note that ϕ now depends on the type of atom i (t_i) and atom j (t_j) and the terms in the j-sum for $\bar{\rho}_i$ each depend on the type of neighbor atom j. Thus, for a binary alloy with atom types A and B, the complete EAM energy expression requires definitions for $\phi_{AA}(r)$, $\phi_{AB}(r)$, $\phi_{BB}(r)$, $\rho_A(r)$, $\rho_B(r)$, $F_A(\bar{\rho})$, and $F_B(\bar{\rho})$.

In fitting an alloy potential of the form in equation (6), one can proceed in two different ways. One approach is to perform a global optimization of all these functions to find the best match (e.g. in a least-squares sense) to a set of experimental properties involving pure A, pure B, and the AB alloy(s). The disadvantage of this approach is that the calculated properties of pure A (or pure B) generally will not be as accurate as when a potential for pure element A is fitted alone. On the other hand, the increased flexibility in the parameter space can result in a better overall description of the alloy system. This approach has been used with considerable success by Foiles *et al.* (1986), who optimized not just two but six different f.c.c. metals and all their binary alloys in a single global optimization. For each binary system (AB), the reference data set consisted of the heat of solution at infinite dilution for A in B and for B in A. This type of procedure could also employ data on ternary alloys, if available from either experiment or first-principles calculations (see Section 4.2).

The other approach is to begin by fitting pure A and pure B, and then constructing the cross-potential $\phi_{AB}(r)$ to obtain the best fit to alloy properties. In this method, one can also consider two transformations under which equation (2) is invariant and equation (5) is not. The first of these corresponds to scaling the density,

$$\rho'_A(r) = s_A \rho_A(r) \tag{7a}$$

$$F'_A(\rho) = F_A(\bar{\rho}/s_A) \tag{7b}$$

where the prime indicates the transformed function. In the other transformation, a linear term is added to $F(\bar{\rho})$,

$$F'_A(\bar{\rho}) = F_A(\bar{\rho}) + g_A \bar{\rho} \tag{8a}$$

$$\phi'_{AA}(r) = \phi_{AA}(r) - 2g_A \rho_A(r) \tag{8b}$$

Because these transformations change the alloy energy without affecting the pure-element energies, they can (and should) be used in the fitting procedure to improve the quality of the alloy potential. Note that the effect of transformations (7) and (8) depends on the order in which they are applied. In the work described below, the linear transformation in equation (8) is applied before the scaling in equation (7). To fit an alloy system with N components (A, B, . . ., X), one determines $N(N-1)/2$ cross-potentials ($\phi_{AB}(r)$, $\phi_{AC}(r)$,. . .), and simultaneously optimizes the $2N-1$ transformation parameters (s_B, s_C, . . ., s_X, and g_A, g_B, . . ., g_X). The parameter s_A is excluded because only the *relative* scaling of the ρ functions affects the alloy energy.

An alternative, simpler approach has been presented by Johnson (1989). Choosing the proper definition for $\phi_{AB}(r)$ in terms of $\phi_{AA}(r)$, $\phi_{BB}(r)$, $\rho_A(r)$ and $\rho_B(r)$, the AB alloy energy becomes invariant to the transformation in equation (8). In this approach, fitting an alloy potential requires only that the $N-1$ ρ-scaling parameters be optimized.

The EAM energy expression for an alloy is identical whether the system is an ordered intermetallic or a random solid solution. The preference for one or the other comes out of the particular definitions for ϕ, ρ, and F, especially the magnitude of $(\phi_{AA}+\phi_{BB})/2$ relative to ϕ_{AB} and that of ρ_A relative to ρ_B.

3. Closely Related Methods

In addition to the effective-medium-based methods (Jacobsen *et al.*, 1987; Stave *et al.*, 1990) discussed in Section 2.2, there are also a few other interatomic potential methods that bear a close resemblance to EAM (Finnis and Sinclair, 1984; Ercolessi, 1983; Ercolessi *et al.*, 1983, 1986; Tománek and Bennemann, 1985; Rosato *et al.*, 1989). Although these potentials were derived from different considerations, the resulting forms are virtually identical to equation (2) for pure elements. It is thus instructive to discuss their origins.

3.1 Second Moment Approximation

The 'N-body potentials' developed by Finnis and Sinclair (1984), and the potentials reported by Tománek and Bennemann (1985), and Rosato *et al.* (1989), correspond to a second moment approximation (SMA) to tight-binding theory. In tight binding theory (Harrison, 1980; Pettifor *et al.*, 1989), atom-based orbitals are assumed to interact via a simple one-electron Hamiltonian. Diagonalizing the Hamiltonian matrix for the system leads to a set of orbital energy levels which can be populated with electrons and summed to obtain the total bonding energy. Expressing the distribution of these energy levels as a density of states (DOS), the bonding energy can be written as

$$E_{bond} = \int_{-\infty}^{E_F} \varepsilon n(\varepsilon) d\varepsilon \tag{9}$$

where $n(\varepsilon)$ is the DOS and E_F is the Fermi level.

If, rather than determining the exact DOS for the system, one approximates the DOS shape from its low-order moments, a drastic reduction in computational work results. This is because it is relatively easy to compute the Hamiltonian moments atom by atom. For example, assuming an s basis (one s orbital per atom), the second moment of the DOS on atom i is given by

$$\mu_{2i} = \langle \chi_i | H^2 | \chi_i \rangle = \sum_j \langle \chi_i | H | \chi_j \rangle \langle \chi_j | H | \chi_i \rangle = \sum_j h_{ij}^2 \quad (10)$$

Here χ_i is the basis function on atom i, $h_{ij} \equiv \langle \chi_i | H | \chi_j \rangle$, and the summation arises from insertion of a complete set of basis functions between the Hamiltonians.

Choosing any basic shape for the DOS, such as a Gaussian or a rectangle, it is easy to show that the width of the DOS is proportional to $(\mu_{2i})^{1/2}$. Ignoring higher moments and assuming $\mu_{1i} = 0$, evaluation of the bonding energy from equation (9) gives

$$E_{\text{bond},i} = -A(\mu_{2i})^{1/2} \quad (11)$$

where A is a positive constant that depends on the chosen DOS shape and the fractional electron occupation.

To obtain an interatomic potential, the approximate tight-binding bond energy should be augmented by a pairwise sum to account for core–core interactions and to correct for double counting. Combining equations (10) and (11), the s-basis SMA energy of atom i thus becomes

$$E_i = \tfrac{1}{2} \sum_j \phi(r_{ij}) - A\left(\sum_j h_{ij}^2(r_{ij})\right)^{1/2} \quad (12)$$

where we have noted that h_{ij} is simply a function of r_{ij}. The correspondence to the EAM expression in equation (2) is now obvious, with

$$\rho(r) \equiv h_{ij}^2(r) \quad (13a)$$

and

$$F(\bar{\rho}) \equiv -A(\bar{\rho})^{1/2} \quad (13b)$$

In this derivation, the embedding function takes on a particular form, namely a negative square root. This has a positive second derivative for all $\bar{\rho}$, consistent with the concept of bond counting discussed in Section 2.2, as expected from its quantum mechanical derivation.

Because this $F(\bar{\rho})$ has negative slope for all values of $\bar{\rho}$, it provides the cohesive force, and must be balanced by a repulsive pair potential. However, the invariance of the EAM energy to the transformations in equations (7) and (8) means that this energy partitioning is not unique.

Traditionally, the SMA has been applied to both f.c.c. and b.c.c. metals, while EAM has been applied predominantly to f.c.c. There is no particular reason to view either approach as better suited for either crystal type, although the restriction that $F(\bar{\rho})$ be a negative square root presumably makes the SMA less flexible. For alloy systems, there is actually a slight formal difference between EAM and SMA arising from the difference in their physical origins. In EAM, the terms in the density sum for atom i in equation (6) depend on the atom type of neighbor j but not on the type of atom i. This is because the fixed density on atom j is independent of atom i. In the corresponding SMA expression (equation (10)), the terms have a different meaning: they are the squares of matrix elements between atom i and atom j, and so depend on the type of both atom i and atom j. In constructing a binary-alloy potential, SMA thus requires one more function ($h_{t_i t_j}(r)$) than EAM.

An appealing aspect of this second-moment view of EAM is that it offers a natural pathway to more accurate potentials. By extending the energy expression to include higher moments, either via the recursion method (Haydock *et al.*, 1972, 1975) or other approaches (Brown and Carlsson, 1985), the intricacies of chemical bonding are more faithfully represented. Higher moments are simply formed from Hamiltonian products that correspond to paths with more atom-to-atom jumps. Using p and d basis functions (rather than just s) puts explicit directionality into the energy. Investigations along these lines are ongoing in a number of research groups (see, e.g., Carlsson, 1989; Carlson *et al.*, 1990; Pettifor, 1989), with the goal of developing the next generation of interatomic potentials that can treat not just metals, but directionally bonded materials as well.

Another bonus of the moment view is the relatively simple physical interpretation. For example, while the second moment counts bonds to immediate neighbors, the improvement contained in the fourth moment can be similarly understood. The fourth moment is a sum over paths with four links. An important part of this sum is the set of paths that go from atom i out to neighbor j, from there to neighbor k, then retracing back through atom j to atom i. This type of path allows the system to sense the number of bonds atom j makes to atoms *other* than i, offering a measure of how much bonding is available to offer to atom i.

This second-moment method is sometimes referred to in the literature as a 'tight binding' formalism, with the discussion of the second moment truncation left to the calculational details section. Given the significant difference between SMA and full tight binding, in terms of both accuracy and computational difficulty, adoption of a clearer terminology would be helpful.

3.2 Glue Model

Ercolessi and co-workers (Ercolessi, 1983; Garofalo, 1984; Ercolessi *et al.*, 1986) developed the 'glue model,' in which a many-body force (the 'glue') augments a pair potential to coax the metal towards the correct coordination number. Their motivation was to obtain a good description of Au, which has a strong propensity toward surface reconstructions that maximize the coordination of the surface-layer atoms. The form of the glue model is exactly the same as in equation (2). Taking a purely empirical approach, the functional shapes were fitted to a host of properties, including the lattice constant, cohesive energy, surface energy, bulk modulus, X-point transverse phonon frequency, vacancy-formation energy, Cauchy pressure, melting temperature, latent heat of fusion, and the thermal expansion coefficient. This is a much larger set of properties than is usually employed in an EAM potential fit. The result is a potential that gives an impressive description of various Au surface reconstructions (Ercolessi *et al.*, 1986) with only a first-nearest-neighbor cutoff distance. The embedding function has a negative curvature for small $\bar{\rho}$ and a minimum (and positive curvature) at the equilibrium $\bar{\rho}$.

Because EAM is a central potential, third-neighbor interactions are required to distinguish f.c.c. and h.c.p. crystal structures, just as for a pair potential. This first-neighbor glue model for Au thus cannot distinguish f.c.c. from h.c.p., but this disadvantage is offset by the fact that the first-neighbor cutoff makes the energy and derivative evaluation very fast.

4. EAM Potential for the Ni–Al–B System

Having discussed the form of the EAM, we now show by example how one proceeds in fitting a potential.

The approach used by most groups, and the one demonstrated here, is to seek the best possible fit to experimental data, relying on the physical underpinnings of equation (2) to give a potential that is reasonable in other parts of configuration space. This empirical approach, while perhaps less satisfying than attempting to derive functional shapes from first principles, has worked quite well and has contributed to the widespread use of EAM for metal and alloy simulations.

The Ni–Al–B potential described in this section (Voter and Chen, 1987; Voter *et al.*, 1989) was constructed to study Ni, Al, and $L1_2$ Ni_3Al grain boundaries with and without boron (Chen *et al.*, 1989, 1990). For this reason, little effort was put into making the Ni–Al potential suitable for stoichiometries other than pure Ni, pure Al, and Ni_3Al, although it has since been used with some success for B2-phase NiAl (Moncevicz *et al.*, 1991; Clapp *et al.*, 1989). The description of pure B is expected to be inadequate, as real B exhibits significant directionality in its bonding, but EAM should give a reasonable description of B embedded in a metallic substrate at low concentrations.

EAM potentials for the Ni–Al system have also been constructed by Foiles and Daw (1987), Vitek *et al.* (1990), Brown and Johnson (1991), and Rao *et al.* (1991).

4.1 Fitting the Pure Elements

The pairwise interaction is taken to be a Morse potential,

$$\phi(r) = D_M\{1 - \exp[\alpha_M(r - R_M)]\}^2 - D_M \qquad (14)$$

where the three parameters, D_M, R_M, and α_M, define the depth and position of the minimum, and a measure of the curvature at the minimum, respectively. The density function is taken as the density of a hydrogenic 4s orbital

$$\rho(r) = r^6(e^{-\beta r} + 2^9 e^{-2\beta r}) \qquad (15)$$

where β is an adjustable parameter. Because $r^6e^{-\beta r}$ turns over at short r, the second term has been added to maintain the monotonically decreasing character of $\rho(r)$ to shorter r (r values inside the maximum are forbidden in the simulations). To ensure that the interatomic potential and its first derivatives are continuous, both $\phi(r)$ and $\rho(r)$ are smoothly cut off at $r = r_{cut}$ by using

$$h_{smooth}(r) = h(r) - h(r_{cut}) + \left(\frac{r_{cut}}{m}\right)\left[1 - \left(\frac{r}{r_{cut}}\right)^m\right]\left(\frac{dh}{dr}\right)_{r=r_{cut}}, \qquad (16)$$

where $h(r) = \phi(r)$ or $\rho(r)$ and $m = 20$; r_{cut} is used as a fitting parameter. Following Foiles (1985a), $F(\bar{\rho})$ is

defined by requiring that the energy of the f.c.c. crystal vs. lattice constant is given by the universal energy form of Rose *et al.* (1984),

$$E_U(a^*) = -E_{coh} f(a^*) \tag{17}$$

where

$$f(a^*) = (1 + a^*)e^{-a^*} \tag{18}$$

Here E_{coh} is the crystal cohesive energy (per atom) and a is a reduced lattice constant defined by

$$a^* = (a/a_0 - 1)/(E_{coh}/9B\Omega)^{1/2} \tag{19}$$

where a is the lattice constant, a_0 is the equilibrium lattice constant, B is the bulk modulus, and Ω is the equilibrium atomic volume. Thus, knowing E_{coh}, a_0, and B, the embedding function is defined by requiring that the crystal energy from equation (2) matches E_U from equation (17) for all values of a^*. The crystal energy needs to be zero when the crystal nearest-neighbor distance reaches r_{cut} (i.e. when $a^* = a^*_{cut}$). This is accomplished by modifying the universal function in a manner suggested by Foiles (1985b),

$$f_{mod}(a^*) = \frac{f[(1-\epsilon)^{1/2}a^*] - \epsilon}{1 - \epsilon} \tag{20}$$

where $\epsilon = f[a^*_{cut}]$. To make E_U go to zero at *exactly* a^*_{cut} requires shifting ϵ slightly. Defining q by

$$\epsilon = f(q) \tag{21}$$

we can solve iteratively for q using

$$q_{n+1} = \tfrac{1}{2}\{q_n + [1 - f_{mod}(q_n)]^{1/2} a^*_{cut}\} \tag{22}$$

with $q_1 = a^*_{cut}$ as a starting guess.

Having defined the functional forms, we now describe the fitting procedure. The five parameters defining $\phi(r)$ and $\rho(r)$ (D_M, R_M, α_M, β, and r_{cut}) are optimized by minimizing the root-mean-square deviation (χ_{rms}) between the calculated and reference properties of the material. Because $F(\bar{\rho})$ is redefined for each choice of the parameters, the potential always gives perfect agreement with the experimental values of a_0, E_{coh}, and B. For Ni and Al, the reference properties are the three cubic elastic constants (C_{11}, C_{12}, and C_{44}), the vacancy-formation energy (E^f_{vac}), and the bond length (R_e) and bond strength (D_e) of the diatomic molecule. In addition, the h.c.p. and b.c.c. crystal structures are required to be less stable than f.c.c. Because the function being minimized contains discontinuities (such as when the wrong crystal structure becomes more stable) and many local minima, the parameter space is searched using the very robust (albeit slow) simplex algorithm (Nelder and Mead, 1965). The best fits for Ni and Al are shown in Table 1, the resulting parameter sets are shown in Table 2, and the functional shapes are displayed in Figure 1. The fit for Ni is excellent, with $\chi_{rms} = 0.75\%$, while the fit for Al is not quite as good, with $\chi_{rms} = 3.85\%$.

Owing to the complex structure of the native rhombohedral phase of boron, we simplify the fitting procedure by treating B as an f.c.c. material. Because experimental measurements are not available for f.c.c. B, we turn to high quality electronic structure calculations. The linearized muffin-tin orbital (LMTO) approach (Andersen, 1975; Skriver, 1984), based on the local density approximation, can be used to compute the binding energy of a crystal as a function of lattice constant. From a set of these calculations, the equilibrium ($T = 0$) values for a_0, E_{coh}, and B can be predicted to good accuracy, as demonstrated for NiAl and Ni_3Al (Chen *et al.*, 1990). (Band structure calculations are also described in Chapter 6 by Singh in this volume.) The f.c.c. structure is used as the 'native' form, from which $F(\bar{\rho})$ is constructed. LMTO results on the b.c.c. structure and f.c.c. with one atom (out of four) missing per unit cell ('f.c.c.(3/4)') are used to provide data for the least-squares search. The results of this fit are included in Table 1.

4.2 Fitting the Cross Potentials

The cross potentials are fitted as described in Section 2.2. The pair potentials ($\phi_{Ni\text{-}Al}(r)$, $\phi_{Ni\text{-}B}(r)$, $\phi_{Al\text{-}B}(r)$) are each defined as a Morse function with a cutoff. The Ni–Al interaction is found first, by optimizing the four Morse parameters and the transformation parameters (s_{Al}, g_{Ni}, and g_{Al}) in a fit to a variety of experimental data on $L1_2$ Ni_3Al and B2 NiAl. For Ni_3Al these quantities are a_0, E_{coh}, E_{vac}, the elastic constants, the (1 1 1) and (1 0 0) antiphase-boundary (APB) energies and the superlattice intrinsic stacking fault (SISF) energy. For B2 NiAl, only a_0 and E_{coh} were included. The results of this fit are shown in Table 3. Next, the Ni–B cross-potential is found by optimizing the Morse parameters for $\phi_{Ni\text{-}B}$ and the transformation parameters s_B and g_B. The set of reference data for these are once again obtained exclusively from LMTO, using the hypothetical $L1_2$ Ni_3B and B2 NiB structures.

Table 1. Properties used in fit to f.c.c. Ni, Al, and B. Calculated values of a_0 E_{coh}, and B match experiment exactly owing to the way $F(\rho)$ is determined. The LMTO results are from Chen *et al.* (1990). The experimental data on the diatomic boron molecule are from Huber and Hertzberg (1979). The other experimental references can be found in Voter and Chen (1987)

		Ni		Al		B	
Structure	Property	Expt.	Calc.	Expt.	Calc.	Expt.	Calc.
f.c.c.	a_0 (Å)	3.52		4.05		2.91	
	E_{coh} (eV)	4.45		3.36		5.33	
	$B(10^{12}$ erg cm$^{-3})$	1.81		0.79		2.02	
	$C_{11}(10^{12}$ erg cm$^{-3})$	2.47	2.44	1.14	1.07		
	$C_{12}(10^{12}$ erg cm$^{-3})$	1.47	1.49	0.619	0.652		
	$C_{44}(10^{12}$ erg cm$^{-3})$	1.25	1.26	0.316	0.322		
	ΔE^f_{1v} (eV)	1.60	1.60	0.75	0.73		
	D_e (eV)	1.95	1.94	1.60	1.54	1.59	1.62
	R_e (Å)	2.2	2.23	2.47	2.45	3.08	3.27
b.c.c.	a_0 (Å)					2.34	2.33
	E_{coh} (eV)					4.95	5.31
	$B(10^{12}$ erg cm$^{-3})$					2.11	2.12
f.c.c.(3/4)	a_0 (Å)					2.78	2.65
	E_{coh} (eV)					5.78	5.66
	χ_{rms} (%)		0.75		3.85		4.12

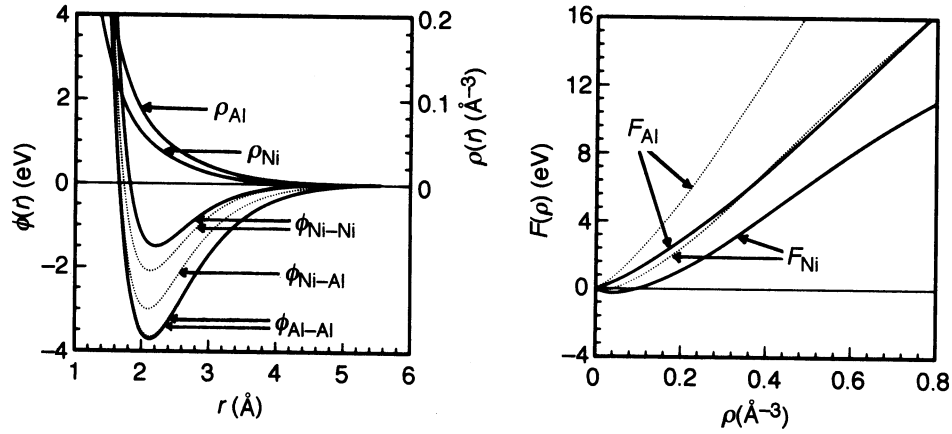

Figure 1. The functions comprising the Ni_3Al potential. The ρ_{Al} curve has been scaled by s_{Al}. Where two curves are displayed, the dotted one represents the function after the transformations of equations (7) and (8) have been applied

Table 2. Potential parameters for f.c.c. Ni, Al, and B, optimized from data in Table 1

	Ni	Al	B
D_M (eV)	1.5335	3.7760	0.7182
R_M (Å)	2.2053	2.1176	1.6517
α_M (Å^{-1})	1.7728	1.4859	3.1915
β (Å^{-1})	3.6408	3.3232	2.0108
r_{cut} (Å)	4.7895	5.5550	4.3716

Finally, the Morse parameters for ϕ_{Al-B} are optimized to find the Al–B cross-potential. For ϕ_{Al-B}, fixing r_{cut} at 3.0 Å and using $D_e = 1.60$ eV helps to control the fit. The results of the Ni–B and Al–B fits are shown in Table 4 and are seen to be quite good. The optimized parameters are in Table 5.

An alternative procedure, which we have not tried, would be to fit all the cross-pair-potentials and

Table 3. Properties used to fit the Ni–Al cross-potential. References for the experimental data can be found in Voter and Chen (1987)

	Properties	Expt.	Calc.
Ni_3Al	a_0 (Å)	3.567	3.573
	E_{coh} (eV)	4.57	4.59
	C_{11} (10^{12} erg cm^{-3})	2.30	2.46
	C_{12} (10^{12} erg cm^{-3})	1.50	1.37
	C_{44} (10^{12} erg cm^{-3})	1.31	1.23
	ΔE^f_{1v} (eV)	1.6 ± 0.2	1.64(Ni) 1.87(Al)
	SISF(1 1 1) (mJ m^{-2})	10 ± 5	13
	APB(1 0 0) (mJ m^{-2})	140 ± 14	83
	APB(1 1 1) (mJ m^{-2})	180 ± 30	142
B2 NiAl	a_0 (Å)	2.88	2.87
	E_{coh} (eV)	4.51	4.38

Table 4. Properties used to fit the Ni–B and Al–B cross-potentials. LMTO results are from Chen *et al.* (1990)

	Properties	LMTO	Calc.
Ni_3B ($L1_2$)	a_0 (Å)	3.39	3.39
	E_{coh} (eV)	4.80	4.80
	B (10^{12} erg cm^{-3})	2.56	2.56
NiB (B2)	a_0 (Å)	2.55	2.58
	E_{coh} (eV)	5.30	5.30
Al_3 ($L1_2$)	a_0 (Å)	3.805	3.909
	E_{coh} (eV)	3.72	3.92
	B (10^{12} erg cm^{-3})	9.27	9.22
AlB (B2)	a_0 (Å)	2.96	0.96
	E_{coh} (eV)	4.24	4.27

transformation parameters in a single optimization. This would put the Ni–B and Al–B cross-potentials on an equal footing with the Ni–Al cross-potential.

It is worth noting that constructing high-quality Ni–B and Al–B cross-potentials would have been virtually impossible without the use of electronic-structure results. Augmenting experimental data with theoretical calculations on hypothetical crystal structures is gaining popularity as a powerful tool in fitting potentials.

Table 5. Optimized parameters for the Ni–Al, Ni–B, and Al–B cross-potentials

	ϕ_{Ni-Al}	ϕ_{Ni-B}	ϕ_{Al-B}
D_M (eV)	3.0322	0.28223	0.12949
R_M (Å)	2.0896	2.3149	2.8876
α_M (Å^{-1})	1.6277	2.4852	1.3904
r_{cut} (Å)	5.4639	2.8181	3.0000
	Ni	Al	B
s_x	1.0	0.61723	3.4936×10^{-3}
g_x (eV Å^3)	6.51451	−0.22050	−0.078785

5. Example Calculations

Atomistic simulations can be applied to a wide range of defects and dynamical processes, limited only by the computer capacity, as discussed in Section 1. The properties that can be studied are those that derive from knowing the system energy as a function of atomic configuration, such as point and planar defect structures, defect energies, free-energy differences, elastic properties, stress distributions, diffusion constants, phonon spectra, and phase transitions.

As discussed in Section 2.2, because of the physical underpinnings of the EAM, it gives a reasonable description of defect structures and energies. The goal of this section is to give some sense of what can be done with atomistic simulations using EAM potentials, by discussing a few examples.

5.1 Free Surfaces

Perhaps the best illustration of the predictive power of EAM comes from an examination of the relaxations and reconstructions that occur at free surfaces. At a metal surface, the first layer of atoms generally contracts toward the second layer relative to the bulk spacing. Using EAM concepts, this is easy to understand. The atoms at the surface have fewer bonds than in the bulk, and consequently move toward the bulk to resaturate their bonding. However, the atoms in the second layer (or a deeper layer, depending on the geometry of the crystal face) now see more density (bonding) than the bulk value. To correct this, the spacing between layer two and layer three *increases*. This effect continues, resulting in oscillatory relaxations that persist for many layers into the bulk. EAM provides not only an understanding of this phenomenon, but can offer relatively accurate predictions of the interlayer spacings (Chen *et al.*, 1986, 1987b). Additional features arise when the surface is that of an ordered intermetallic. The interested reader is referred to Chapter 25 by Farkas in this volume, which treats this topic in detail and includes results using the Ni–Al potential presented in Section 4.

5.2 Boron Interstitial in Ni_3Al at Bulk and Grain-Boundary Sites

Interest in boron in Ni_3Al stems from the observation that very small concentrations of B can produce ductility in polycrystalline Ni_3Al, which is otherwise extremely brittle (Aoki and Izumi, 1979). It is still an unresolved

question whether the primary effect of the boron is to strengthen the grain boundaries or improve the plasticity at the boundaries.

Using molecular-statics calculations with EAM potentials, it is possible to address questions about the relative stabilities and structures of possible boron sites. Molecular statics refers to the procedure of finding the atomic geometry that corresponds to the lowest energy for a given defect specification. These energies and structures thus correspond to the classical zero-temperature system, representing a good approximation at low to moderate temperatures. If accurate results are desired for a specific nonzero temperature, Metropolis Monte Carlo (Metropolis *et al.*, 1953) or molecular dynamics can be employed to study the appropriate constant-temperature ensemble.

Considering bulk interstitial boron, there are three possible sites: a tetrahedral site and two octahedral sites. In the tetrahedral site, the nearest neighbors of the B are one Al and three Ni atoms (3Ni–1Al), while the two octahedral sites correspond to 6Ni and 4Ni–2Al neighbor patterns. To study this system, a 256-atom block of $4\times4\times4$ unit cells of $L1_2$ Ni_3Al with periodic boundary conditions was employed. Placing the single B atom in one of the candidate sites, the energy was determined by relaxing both the system dimensions and the individual atom positions of all 257 atoms. The 6Ni octahedral site is found to be the most stable, with an energy of -4.59 eV (relative to an isolated B atom and an unperturbed Ni_3Al crystal) and a formation volume of 15.8 Å $= 1.4\,\Omega$. The 4Ni–2Al octahedral site is at -3.65 eV and the 3Ni–1Al tetrahedral site is at -2.99 eV. These results are consistent with the conclusion from channeling/nuclear-reaction analysis that the B resides in one of the two octahedral sites (Bohn *et al.*, 1987).

It is interesting to examine the relative contributions of the different relaxations to the final energy. With the B placed on the symmetric position in the 6Ni octahedral site, before any relaxation, the energy is positive ($+3.35$ eV). Relaxing only the first shell of six Ni atoms lowers the energy by 7.3 eV, while all further relaxations combined account for only 0.63 eV. The majority of this 0.63 eV comes from the relaxation of the third-neighbor shell (0.48 eV). The first shell of six Ni atoms relaxes outward by 0.28 Å, the second shell of eight Al atoms relaxes *inward* by 0.001 Å, and the third shell of 24 Ni atoms relaxes outward by 0.07 Å. After all 257 atom positions are relaxed individually, scaling the system size (i.e. the volume relaxation) lowers the energy by only 0.05 eV, and re-relaxing the atom positions has no noticeable effect on the energy. Thus, a very good estimate of the interstitial formation energies can be obtained by simply relaxing a few neighbor shells.

Molecular statics can also be used to investigate the tendency for B to segregate to a grain boundary (GB). Examining various possible interstitial sites at the GB leads to energies as low as -6.9 eV. (Chen *et al.*, 1990), consistent with the experimental observation that boron segregates to the grain boundaries (White *et al.*, 1985). This energy lowering relative to the bulk interstitial occurs because the defective nature of the GB offers sites with less crowding by the neighboring atoms. In addition, it is found that B at the GB reduces the Ni antisite defect energy, causing a co-segregation effect. In Ni-rich polycrystals, the excess Ni favors replacing the Al at a boron-rich GB over replacing Al in the bulk (Chen *et al.*, 1990). See also the chapter by Takasugi.

5.3 Grain Boundary Cohesion in Ni_3Al

To study grain-boundary strength, there are (at least) three approaches that can be used. The simplest is to examine the Griffith cohesive energy, defined as the energy required per unit area to cleave a brittle material without plastic deformation (Griffith, 1920). This is easily computed from the results of molecular-statics simulations on the GB of interest and the free surfaces that would result from perfect cleavage along the boundary. Using the EAM potential presented above, this type of simulation showed that the grain-boundary cohesion in Ni_3Al is comparable to that for pure Ni, indicating that the brittleness of polycrystalline Ni_3Al does not arise from an intrinsic GB weakness (Chen *et al.*, 1987a; Chen *et al.*, 1989).

A more sophisticated approach, which allows plastic deformation in a very limited, local sense, is the stepwise relaxation method. Using clamps in the model, the crystal is strained normal to the GB in a stepwise fashion, using molecular statics to reminimize the energy after each step. In addition to providing the GB cohesive energy, which may or may not be the same as the Griffith value, this method also allows calculation of the stress at each step, so that a stress–strain curve can be constructed. Although the sequence of configurations does not correspond to any physically realizable process, the procedure offers a well-defined, easily computed approximation to the actual boundary cleavage event. Using this approach, Chen *et al.* (1990) showed that introduction of boron at the (2 1 0) or (3 1 0) boundaries ((1 0 0)-tilt GB series) increased both the maximum stress and the total work required for cleavage. The effect was

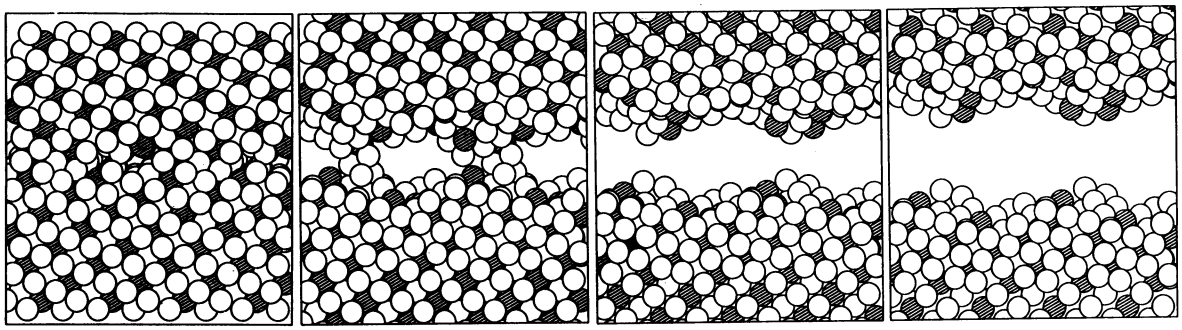

Figure 2. Time sequence of snapshots from molecular-dynamics simulation of the (1 0 0)-tilt, (2 1 0) grain boundary of Ni_3Al at $T = 300$ K. Clamped regions at the top and bottom move apart at a constant velocity corresponding to an initial engineering strain rate of $5 \times 10^{10}\ s^{-1}$ at time $t = 0$. Two simulation periods are shown. The successive images are at strains of 20, 40, 60, and 80%

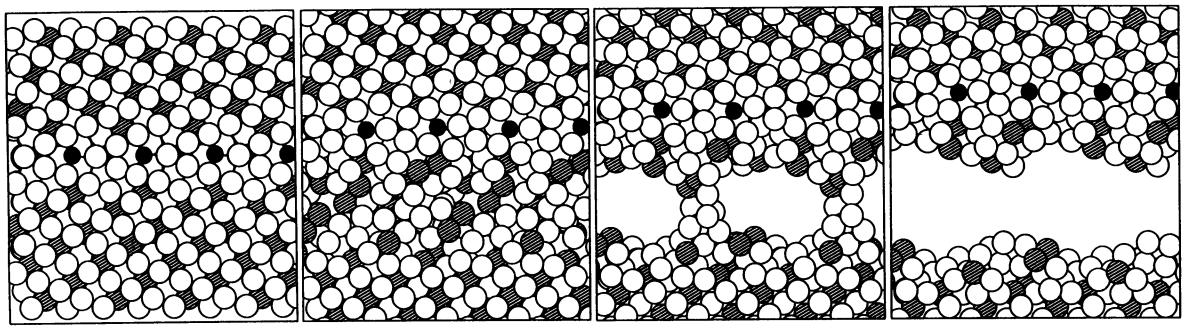

Figure 3. Time sequence of snapshots from molecular-dynamics simulation. Conditions are exactly as as Figure 2, except that the grain boundary has been modified by the addition of interstitial boron and substitutional nickel

especially pronounced when some of the Al atoms at the GB were replaced with Ni atoms, to approximate the co-segregation effect discussed above.

The third approach is the use of molecular dynamics (MD) to examine the dynamical behavior of the loaded boundary as it cleaves. This method, while more computationally intensive, has the advantage that it does correspond to a real physical event, although experimentally it may be impossible to observe it directly. A simulation of the cleavage of the (2 1 0) GB of Ni_3Al with and without boron is presented here as an example. The simulation block consists of about 400 atoms, with periodic boundary conditions in the two Cartesian directions parallel to the GB plane. In the direction normal to the GB, the strain is increased to cause cleavage. This is accomplished by specifying a fixed velocity for the outermost layers of atoms, corresponding to a desired strain rate. These velocities are not updated during the simulation, so the system acts as if it is attached to clamps moving apart at a constant velocity. Before the strain is applied, the system is 'warmed up' to $T = 300$ K, using a thermostat. After the clamps begin moving, the few layers of atoms near the clamps are still controlled by a thermostat, while the atoms around the GB evolve according to unperturbed classical equations of motion.

The strain rate in the simulations presented here is $5 \times 10^{10}\ s^{-1}$. Although this is many orders of magnitude faster than macroscopic strain rates in controlled fracture experiments, it may not be an unreasonable value for the *local* strain rate experienced in the region of the GB as the local stress achieves the critical value necessary to begin cleavage. This hypothesis can be tested by replacing the constant-strain-rate boundary conditions with constant-stress boundary conditions.

Figure 2 shows snapshots from a simulation on an undoped GB, while Figure 3 shows the same GB enriched with interstitial boron and some substitutional Ni atoms (consistent with the co-segregation effect discussed in Section 5.2). The qualitative difference in behavior is obvious. While the boron-free GB cleaves along the boundary plane, the boron- and

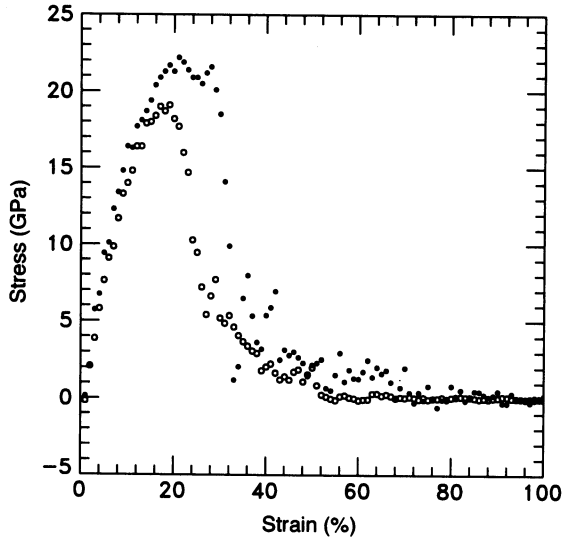

Figure 4. Local stress vs. local strain for the Ni_3Al molecular-dynamics simulations shown in Figures 2 and 3. The open circles represent the pure Ni_3Al case, while the full circles are for the boron-doped case

nickel-enriched GB cleaves *in the bulk*, leaving the GB intact. Figure 4 shows the tensile stress as a function of time for the two cases. Consistent with the qualitative behavior, the maximum stress for the enriched boundary is ~22 GPa, while the clean boundary fails at a lower value of ~19 GPa. Moreover, integrating the curves indicates that 44% more work is required to cleave the enriched boundary. It is interesting to note that the maximum stress values for these two boundaries are very similar (within 1 or 2 GPa) to those obtained using the simpler stepwise relaxation method.

Because these simulations were performed on fairly small systems, the quantitative accuracy of the results is questionable. For example, the cleavage path in Figure 3 runs very close to the thermostat region adjacent to the lower clamp. A systematic study of the dependence on system size (in all three directions) and strain rate would be very useful. However, the qualitative conclusion seems clear: for this EAM model of Ni_3Al, a GB with segregated B and Ni has a substantially increased resistance to cleavage.

6. Applicability of EAM to Other Intermetallics

In addition to studies of the $L1_2$ (cP4) structure Ni_3Al (e.g. see Yoo *et al.*, 1989; Parthasarathy *et al.*, 1991; Lin and Chen, 1990; Pestman *et al.*, 1990; Vitek *et al.*, 1990; Najafabadi *et al.*, 1991; Mills *et al.*, 1991; Foiles *et al.* 1991; Vitek, 1992) and B2 (cP2) NiAl (e.g. see Clapp *et al.*, 1989; Pasianot and Farkas, 1990; Moncevicz *et al.*, 1991; Rao *et al.*, 1991) the embedded-atom method has been applied to a few other intermetallic systems, such as $L1_2$ (cP4) Cu_3Au (e.g. see Foiles, 1987; Ackland and Vitek, 1989; Pestman *et al.*, 1991; Wallace and Ackland, 1992), $L1_0$ (tP4) TiAl (Rao *et al.*, 1991), CuTi (Shoemaker *et al.*, 1990; Sabochick and Lam, 1990, 1991), B2(cP2) NiTi (Lutton *et al.*, 1991), B2 (cP2) FeTi (Lutton *et al.*, 1991), and CuNi superlattices (Dodson, 1988; Mintmire, 1990).

EAM should also work well for many other intermetallics (Redfield and Zangwill, 1989), particularly those with the relatively simple structures. Intermetallics with large, complex unit cells probably require a potential with a more sophisticated many-body term that can achieve a longer effective range. This assumption has not yet been thoroughly tested, however, and EAM may prove more powerful than expected in this regard. For advanced intermetallic compounds involving strongly covalent elements, such as $MoSi_2$, EAM is almost certainly inadequate, as it cannot describe directional bonding. For these systems, and for the metal–metal intermetallics with complicated structures, new potential forms will be required.

7. Conclusions

In the last decade, the embedded-atom method has grown from its effective-medium-theory origins to become the interatomic potential of choice for the study of metals and intermetallics. Compared to the previous generation of pair potentials, EAM offers improvements in both accuracy and the capacity for physical interpretation. As a consequence, more researchers than ever perform simulations with the expectation that they will obtain meaningful results. This, in turn, has fostered a broader awareness of the power of atomistic simulations in materials-science problems.

While EAM is capable of describing covalent impurities in low concentration (as shown for the Ni–Al–B system), its spherically symmetric nature is not appropriate for strongly covalent systems. Because many of the advanced intermetallics fall into this category, the next decade should see significant advances in more advanced potential forms. In addition, first-principles methods will continue to evolve, with the long-term promise of yielding highly accurate results for arbitrary systems. Nonetheless, there will still be a place for the computationally fast, n-scaling EAM approach,

because even the fastest of the more advanced potentials will probably be 10 to 100 times slower. For this reason, EAM development will continue, leading to potentials that achieve higher accuracy and describe a broader range of intermetallic alloys.

8. Acknowledgements

The author is grateful to S. P. Chen, D. J. Srolovitz, P. J. Hay, A. M. Boring, and R. C. Albers for collaborations that led to much of the work reported here, to J. J. Eberhardt for championing the materials by design project, and to J. D. Kress for discussions helpful in the preparation of this chapter. This work was supported by the US Department of Energy (DOE) Contract No. W-7405-36. Much of this work was supported by the Energy Conversion and Utilization Technologies (ECUT) Division of the DOE.

9. References

Ackland, G. J., and Vitek, V. (1989). *Mater. Res. Soc. Symp. Proc.*, **133**, 105.

Andersen, O. K. (1975). *Phys. Rev.*, **B12**, 3060.

Aoki, K., and Izumi, O. (1979). *Nippon Kinzoku Gakkaishi*, **43**, 1990.

Bohn, H. G., Williams, J. M., Barrett, J. H., and Liu, C. T. (1987). *Mater. Res. Soc. Symp. Proc.*, **81**, 127.

Brown, J. R., and Johnson, R. A. (1991). *Mater. Res. Soc. Symp. Proc.*, **209**, 71.

Brown, R. H., and Carlsson, A. E. (1985). *Phys. Rev.*, **B32**, 6125.

Carlsson, A. E. (1989). In *Atomistic Simulation of Materials: Beyond Pair Potentials* (eds V. Vitek, and D. J. Srolovitz). Plenum, New York, p. 103.

Carlsson, A. E., Fedders, P. A., and Myles, C. W. (1990). *Phys. Rev.*, **B41**, 1247.

Chen, S. P., Voter, A. F., and Srolovitz, D. J. (1986). *Phys. Rev. Lett.*, **57**, 1308.

Chen, S. P., Voter, A. F., and Srolovitz, D. J. (1987a). *Mater. Res. Soc. Symp. Proc.*, **81**, 45.

Chen, S. P., Voter, A. F., and Srolovitz, D. J. (1987b). *Mater. Res. Soc. Symp. Proc.*, **82**, 515.

Chen, S. P., Srolovitz, D. J., and Voter, A. F. (1989). *J. Mater. Res.*, **4**, 62.

Chen, S. P., Voter, A. F., Albers, R. C., Boring, A. M., and Hay, P. J. (1990). *J. Mater. Res.*, **5**, 955.

Clapp, P. C., Rubins, M. J., Charpenay, S., Rifkin, J. A., Yu, Z. Z., and Voter, A. F. (1989). *Mater. Res. Soc. Symp. Proc.*, **133**, 29.

Clementi, E., and Roetti, C. (1974). *At. Data Nucl. Data Tables*, **14**, Nos. 3 and 4.

Daw, M. S. (1989). *Phys. Rev.*, **B39**, 7441.

Daw, M. S., and Baskes, M. I. (1983). *Phys. Rev. Lett.*, **50**, 1285.

Daw, M. S., and Baskes, M. I. (1984). *Phys. Rev.*, **B29**, 6443.

Dodson, B. W. (1988). *Phys. Rev.*, **B37**, 727.

Ercolessi, F. (1983). PhD thesis, University of Trieste.

Ercolessi, F., Tosatti, E., and Parrinello, M. (1986). *Phys. Rev. Lett.*, **57**, 719.

Finnis, M. W., and Sinclair, J. E. (1984). *Phil. Mag.*, **A50**, 45; (1986). *Phil. Mag.*, **A53**, 161 (Erratum).

Foiles, S. M. (1985a). *Phys. Rev.*, **B32**, 7685.

Foiles, S. M. (1985b). Private communication.

Foiles, S. M. (1987). *Surf. Sci.*, **191**, 329.

Foiles, S. M., and Daw, M. S. (1987). *J. Mater. Res.*, **2**, 5.

Foiles, S. M., Baskes, M. I., and Daw, M. S. (1986). *Phys. Rev.*, **B33**, 7983.

Foiles, S. M., Baskes, M. I., and Daw, M. S. (1989). *Mater. Sci. Forum*, **37**, 223.

Garofalo, M. (1984). Thesis, International School for Advanced Studies, Trieste.

Griffith, A. A. (1920). *Phil. Trans. R. Soc.*, **A221**, 163.

Harrison, W. A. (1966). *Pseudopotentials in the Theory of Metals*. Benjamin, New York.

Harrison, W. A. (1980). *Electronic Structure and the Properties of Solids*. Freeman, San Francisco.

Haydock, R., Heine, V., and Kelly, M. J. (1972). *J. Phys.*, **C5**, 2845.

Haydock, R., Heine, V., and Kelly, M. J. (1975). *J. Phys.*, **C8**, 2591.

Hohenberg, P., and Kohn, W. (1964). *Phys. Rev.*, **B136**, 864.

Huber, K. P., and Hertzberg, G. (1979). *Molecular Spectra and Molecular Structure*, Vol. IV, *Constants of Diatomic Molecules*. Van Nostrand Reinhold, New York, p. 64.

Jacobsen, K. W., Norskov, J. K., and Puska, M. J. (1987). *Phys. Rev.*, **B35**, 7423.

Johnson, R. A. (1989). *Phys. Rev.*, **B39**, 12554.

Kress, J. D., and DePristo, A. E. (1987). *Phys. Rev.*, **B87**, 4700.

Kress, J. D., and DePristo, A. E. (1988). *Phys. Rev.*, **B88**, 2596.

Lin, D., and Chen, D. (1990). *Mater. Res. Soc. Symp. Proc.*, **193**, 265.

Lutton, R. T., Sabochick, M. J., and Lam, N. Q. (1991). *Mater. Res. Soc. Symp. Proc.*, **209**, 207.

Manninen, M. (1986). *Phys. Rev.*, **B34**, 8486.

Metropolis, N., Rosenbluth, A., Rosenbluth, M. N., Teller, A., and Teller, E. (1953). *J. Chem. Phys.*, **21**, 1087.

Mills, J. J., Goods, S. H., and Foiles, S. M. (1991). *Mater. Res. Soc. Symp. Proc.*, **213**, 423.

Mills, J. J., Goods, S. H., Foiles, S. M., and Whetstone, J. R. (1991). *Scripta Metall. Mater.*, **25**, 1283.

Mintmire, J. W. (1990). *Mater. Sci. Eng.*, **A126**, 29.

Moncevicz, A., Clapp, P. C., and Rifkin, J. A. (1991). *Mater. Res. Soc. Symp. Proc.*, **209**, 213.

Najafabadi, R., Wang, H. Y., Srolovitz, D. J., and LeSar, R. (1991). *Mater. Res. Soc. Symp. Proc.*, **213**, 51.

Nelder, J. A., and Mead, R. (1965). *Comput. J.*, **7**, 308.

Norskov, J. K. (1982). *Phys. Rev.*, **B26**, 2875.
Norskov, J. K., and Lang, N. D. (1980). *Phys. Rev.*, **B21**, 2131.
Parthasarathy, T. A., Dimiduk, D. M., Woodward, C., and Diller, D. (1991). *Mater. Res. Soc. Symp. Proc.*, **213**, 337.
Pasianot, R., and Farkas, D. (1990). *Mater. Res. Soc. Symp. Proc.*, **186**, 259.
Pestman, B. J., De Hosson, Th.M., Vitek, V., Tichelaar, F. D., and Schapink, F. W. (1990). *Mater. Res. Soc. Symp. Proc.*, **186**, 253.
Pestman, B. J., De Hosson, Th.M., Vitek, V., and Schapink, F. W. (1991). *Mater. Res. Soc. Symp. Proc.*, **213**, 429.
Pettifor, D. G. (1989). *Phys. Rev. Lett.*, **63**, 2480.
Pettifor, D. G., Skinner, A. J., and Davies, R. A. (1989). In *Atomistic Simulation of Materials: Beyond Pair Potential* (eds V. Vitek, and D. J. Srolovitz). Plenum, New York, p. 317.
Puska, M. J., Nieminen, R. M., and Manninen, M. (1981). *Phys. Rev.*, **B24**, 3037.
Rao, S. I., Woodward, C., and Parthasarathy, T. A. (1991). *Mater. Res. Soc. Symp. Proc.*, **213**, 125.
Redfield, A. C., and Zangwill, A. (1989). In *Atomistic Simulation of Materials: Beyond Pair Potentials* (eds V. Vitek, and D. J. Srolovitz). Plenum, New York, p. 153.
Rosato, V., Guillopé, M., and Legrand, B. (1989). *Phil. Mag.*, **A59**, 321.
Rose, J. H., Smith, J. R., Guinea, F., and Ferrante, J. (1984). *Phys. Rev.*, **B29**, 2963.
Sabochick, M. J., and Lam, N. Q. (1990). *Scripta Metall. Mater.*, **24**, 565.
Sabochick, M. J., and Lam, N. Q. (1991). *Phys. Rev.*, **B43**, 5243.
Shoemaker, J. R., Wesley, D., Wharton, W. R., Oehrli, M. L., Sabochick, M. J., and Lam, N. Q. (1990). *Mater. Res. Soc. Symp. Proc.*, **193**, 339.
Skriver, H. L. (1984). *The LMTO Method*. Springer, Berlin.
Stave, M. S., Sanders, D. E., Raeker, T. J., and De Pristo, A. E. (1990). *J. Chem. Phys.*, **93**, 4413.
Stott, M. J., and Zaremba, E. (1980). *Phys. Rev.*, **B22**, 1564.
Tománek, D., and Bennemann, K. H. (1985). *Surf. Sci.*, **163**, 503.
Vitek, V. (1992). *Prog. Mater. Sci.*, **36**, 1.
Vitek, V., Ackland, G. J., and Cserti, G (1990). *Mater. Res. Soc. Symp. Proc.*, **186**, 237.
Voter, A. F., and Chen, S. P. (1987). *Mater. Res. Soc. Symp. Proc.*, **82**, 175.
Voter, A. F., Chen, S. P., Albers, R. C., Boring, A. M., and Hay, P. J. (1989). In *Atomistic Simulation of Materials: Beyond Pair Potentials* (eds V. Vitek, and D. J. Srolovitz). Plenum, New York, p. 223.
Wallace, W. E., and Ackland, G. J. (1992). *Surf. Sci. Lett.*, **275**, L685.
White, C. L., Padgett, P. A., Liu, C. T., and Yalisov, S. M. (1985). *Scripta Metall. Mater.*, **18**, 1417.
Yoo, M. H., Daw, M. S., and Baskes, M. I. (1989). In *Atomistic Simulation of Materials: Beyond Pair Potentials* (eds V. Vitek, and D. J. Srolovitz). Plenum, New York, p. 401.